"Thin film fuel cells with vanadium oxide anodes: Strain and stoichiometry effects"

Van Overmeere, Quentin ; Ramanathan, Shriram

Abstract

Thin film solid oxide fuel cells incorporating vanadium oxide anodes having open circuit potential of 1 V with hydrogen fuel have been realized. The as-deposited anode stoichiometry was varied by choice of growth conditions of vanadium oxide and a striking correlation to fuel cell performance (open circuit potential and peak power density) is observed. Possible mechanisms leading to the experimental observations based on calculated thermodynamic phase stability under fuel cell operating environments, spectroscopic analysis of the anodes and strain-related arguments are presented.

Document type : *Article de périodique (Journal article)*

Thin film fuel cells with vanadium oxide anodes: strain and stoichiometry effects

Quentin Van Overmeere[1,2], Shriram Ramanathan[1]

[1] School of Engineering and Applied Sciences, Harvard University, Cambridge, MA 02138, USA

[2] Present address: Institute of Mechanics, Materials and Civil Engineering, Université catholique de Louvain, B-1348 Louvain-la-Neuve, Belgium.

E-mail: quentin.vanovermeere@uclouvain.be Tel: +32 10/47.24.18 Address: Place sainte-Barbe 2, B-1348 Louvain-la-Neuve, Belgium.

ABSTRACT

Thin film solid oxide fuel cells incorporating vanadium oxide anodes having open circuit potential of 1 V with hydrogen fuel have been realized. The as-deposited anode stoichiometry was varied by choice of growth conditions of vanadium oxide and a striking correlation to fuel cell performance (open circuit potential and peak power density) is observed. Possible mechanisms leading to the experimental observations based on calculated thermodynamic phase stability under fuel cell operating environments, spectroscopic analysis of the anodes and strain-related arguments are presented.

KEYWORDS Vanadium oxide, thin films, solid oxide fuel cells, phase transformation, anodes

HIGHLIGHTS

- Vanadium oxides of varying stoichiometry have been studied as anodes in thin film solid oxide fuel cells.
- V_2O_3 and V_2O_5 anodes show superior performance.
- Calculated thermal strain and phase stability provide insights into experimental observations.

1. Introduction

Ultra-thin film solid oxide fuel cells allow exploration of operational performance characteristics in the sub-500°C range. Anodes demonstrated to date for such suspended membrane fuel cells include porous metals [1-3], metal-ceramic composites [4] or pure oxides [5]. For freestanding thin film solid oxide fuel cells thinner than 500 nm, open circuit potentials close to the thermodynamic value are generally obtained with porous metal electrodes [1-3]. However, when the cathode and/or the anode consist of entirely dense oxide films, the open circuit potential often decreases below the thermodynamic value. An exception to the lower open circuit potential when using oxide electrodes is when the cathode consists of dense LSCF films [6].

The catalytic activity of vanadium oxide compounds and mixed conductivity are interesting towards exploration as electrodes [7,8]. The vanadium oxide material system is also of broad interest for redox flow cells and batteries [9,10]. In previous work, we identified vanadium dioxide as a candidate anode material; however, the open-circuit potential difference was lower than the thermodynamic value [11]. In this study, we explore this aspect carefully by varying vanadium oxide anode synthesis conditions, which results in differing as-deposited oxide stoichiometry from V metal to V_2O_5. The performance of thin film solid oxide fuel cells varied with the as-deposited vanadium oxide stoichiometry and was the highest for as-deposited V_2O_3 and V_2O_5 anodes. We present our experimental observations and discuss the mechanisms stemming from phase stability and structural changes occurring in the anodes.

2. Experimental

Thin film solid oxide fuel cell freestanding oxide membranes, 160 µm in sidelength, supported on silicon were synthesized with photolithography, KOH anistropic etching of Si and reactive ion etching of Si_3N_4, as described previously [6]. The electrolyte consisted of 100 nm-thick yttria doped zirconia (YSZ) deposited at 823 K from a two inch diameter sintered YSZ target using rf magnetron sputtering at a power of 100 W and pressure of 0.67 Pa. The cathode consisted in a ~80 nm thick

porous platinum film deposited without external heating by DC sputtering with 200 W power at a pressure of 10 Pa to obtain a high density of triple phase boundaries [12]. The anode consisted of ~30 nm thick vanadium oxide synthesized by reactive sputtering from a vanadium metallic target. The oxide stoichiometry was modified by varying the ratio of oxygen to argon, keeping the total volumetric flowrate constant at 24 ml/min. The oxygen fraction was varied over a large range by using either a pure oxygen or a 10% O_2/Ar gas feed. For all the vanadium oxide film compositions in this study, no external heating was applied, the power was 200 W RF and the pressure was kept constant at 0.4 Pa. For all the depositions, the base pressure in the sputtering chamber was better than 10^{-5} Pa. For each anode composition, nine different solid oxide fuel cell membranes were tested. X-ray photoelectron spectroscopy was performed with a Thermo Scientific K-alpha instrument, equipped with an Al-K-α monochromatized x-ray source. The X-ray spot size was 400 µm, except for measurements performed on the anode itself, for which the spot size was 150 µm. The pass energy of the instrument was set to 10 eV for acquisition of the V2p and O1s regions. X-ray diffraction measurements were performed with a Rigaku SmartLab diffractometer, equipped with a 9 kW rotating Cu anode. Measurements were performed at grazing incidence of the source at 0.4° to minimize contributions from the substrate. Thermodynamic calculations of vanadium oxide stability were performed with HSC Chemistry 6.12 [13]. Elemental compositions considered were V, VO, V_2O_3, VO_2 and V_2O_5. The reactions intrinsically considered in the thermodynamic analyses therefore are: $V + ½ O_{2(g)} = VO$, $2 VO + ½ O_{2(g)} = V_2O_3$, $½ V_2O_3 + ½ O_{2(g)} = VO_2$ and $2 VO_2 + ½ O_{2(g)} = V_2O_5$.

3. Results

The deposition of vanadium oxide with different stoichiometry was identified from changes in the deposition rate, measured *in situ* with a quartz crystal microbalance. Different stoichiometries could be identified from discontinuities in the evolution of the deposition rate with oxygen fraction, where different regimes are separated from each other by a hysteresis in the deposition rate, as illustrated in

Figure 1 (a). The hysteresis is due to growth target interactions with oxygen [14]. These different regimes in the deposition rate could be ascribed to the corresponding vanadium oxide stoichiometries using x-ray photoelectron spectroscopy (XPS) and x-ray diffraction (XRD) to identify the valence state of vanadium and the crystalline phase of the film, as shown in Fig. 1 (b) and Fig. 2. Using XPS peak positions from literature and full-width at half-maximum values for the V2p3/2 peak of the different vanadium oxides [15-18], we infer stoichiometries corresponding to V metal, VO, V_2O_3, VO_2 and V_2O_5 respectively for 0, 1, 2.5, 8 and 25 % oxygen in the gas feed during deposition. Additional components in the V2p photoelectron peaks are also present in the XPS spectra for the two lower oxygen fractions. These likely correspond to a thin surface layer of V_2O_3 or VO_2 that forms when the sample is exposed to the ambient atmosphere [19]. The XRD measurements indicate that the film structure for deposition in 0 and 1% oxygen possess peaks corresponding to V metal and VO. No diffraction peaks other than those of the 100 nm-thick YSZ layer on which the VO_x films are deposited are observed for oxygen fractions larger than 1%. This is likely due to the absence of heating during deposition.

The performance of thin film solid oxide fuel cells with 100 nm-thick YSZ electrolyte and 80 nm-thick porous Pt cathode and vanadium oxide anodes of the different stoichiometries ranging from V to V_2O_5 was evaluated from 423 to 713 K with room temperature humidified hydrogen fuel and ambient laboratory air as the oxidant. The average open circuit potential and peak power densities for nine fuel cells patterned on the same silicon chip are shown in Fig. 3 (a) and (b) as a function of temperature and compared against the open circuit potential and peak power density of a benchmark thin film solid oxide fuel cell with porous platinum anode. After loading the cells for evaluating their performance characteristics, steady-state open circuit potentials were recovered within three minutes to pre-load values. Note that fuel cell membranes with open circuit potentials lower than 0.05 V were excluded from the analysis as these could be indicative of a short circuit due to a defective electrolyte rather than an intrinsic feature of the anodes studied here. For all compositions, the open circuit potential at 423 K is considerably lower than 1 V and progressively increases to a first

maximum at about 523 K. For the V_2O_3 and V_2O_5 anodes, the open circuit potential then increases to be closer to the thermodynamic value above 623 K. The open-circuit potential for the vanadium anode is sometimes slightly higher than the open circuit potential for hydrogen oxidation ~1.1 V in the present conditions. We hypothesize this may be due to on-going oxidation of the anode. The cell potential at 600 K, evaluated from the Gibbs free energy of reaction of $V + 0.5\ O_{2(g)} \rightarrow VO$ and $2\ VO + 0.5\ O_{2(g)} \rightarrow V_2O_3$ is respectively equal to 1.95 and 1.59 V. Because the oxidation and thereby consumption of vanadium metal should proceed quickly once current flows, it should be a transient characteristic during fuel cell operation under load. Interestingly, while loading the cell below 573 K resulted in a decrease of the open circuit potential, the initially higher value was recovered within three minutes. Similarly to the open-circuit potential, the peak power density for the V_2O_3 and V_2O_5 anodes shows a transition above 623 K. At 683 K, the best peak power density of the fuel cells with V, VO, V_2O_3, VO_2, V_2O_5 and porous Pt anode are respectively 0.4, 7, 25, 5, 25 and 100 mW/cm^2. The potential difference and power density evolution with current density at ~683 K are shown in Fig. 4. Thus, the best performing fuel cells above 673 K with vanadium oxide anodes have either as-deposited V_2O_3 or V_2O_5 stoichiometry. The apparent activation energy, E_a, for the peak power density of the V_2O_3 anode fuel cells, derived by fitting the peak power density to $\exp(-E_a/(kT))$ in the range 623 to 713 K is equal to 0.72 eV. The activation energy for the peak power density of the porous Pt anode fuel cells is equal to 0.59 eV in the same temperature range. This difference could be due to different rate-limiting steps in the case of V_2O_3 and Pt anode cells. The electrocatalytic activity of platinum is notably high. The composition and structure of surface layers present on the VO_x anodes after their exposure to air, as revealed by XPS for as-deposited V and VO anodes, could influence their electrocatalytic properties and thus the fuel oxidation reaction kinetics. As we discuss later, it is mainly the non-ideal open circuit potential that limits the highest current and power densities attainable here.

To infer if the difference in performance between the anodes is due to their stoichiometry during operation, we performed XPS measurements on the anodes after operation and cool down to room

temperature while continuously flowing humidified 5% H_2 fuel. All spectra were found to be relatively similar, as shown in Figure 5. Two contributions to the V2p3/2 peak can be inferred. The high binding energy contribution corresponds to VO_2, while the lower binding energy contribution at ~515.5 eV may correspond to a vanadium oxide stoichiometry intermediate between V_2O_3 and VO.

4. Discussion

Deviations in the open circuit potential from the thermodynamic value are generally ascribed to short circuits between anode and cathode or fuel crossover through defects in the fuel cell assembly. To first approximation, an open circuit potential decrease by a given factor results in a decrease of the maximum power density by the square of that factor (assuming ohmic losses only, the potential difference V at a current density j is $V = V_{OC} - R\,j$ with V_{OC} and R respectively the open circuit potential difference and the area specific resistance. Deriving the power density vs. j and equating to zero, the maximum power density is $V_{OC}^2/(4R)$). The correlation between open circuit potential difference and peak power density is evident for our different fuel cell anodes. They rank identical when comparing open circuit potential differences and peak power densities at identical temperatures, with the exception of the platinum anode cells which over-perform other cells with open circuit potential differences close to 1 V. Thus, obtaining open circuit potentials as close as possible to the thermodynamic value is naturally important to maximize power density in solid oxide fuel cells. Unlike solid oxide fuel cells that use micron-scale or thicker electrolytes which are well-developed, for thin film solid oxide fuel cells, achieving near ideal open circuit potential differences is not trivial. We hypothesize that the lower open circuit potential when oxide anodes are used in thin film solid oxide fuel cells is due to the generation of subtle structural defects in the electrode/electrolyte thin membrane assembly allowing fuel and oxidant to permeate through the membrane and decrease the open circuit potential difference. These defects could be generated by volumetric changes of oxide-based electrodes during fuel cell operation that can often lead to micro-cracking [20]. Note that thorough examination of the membranes by scanning electron microscopy

and atomic force microscopy did not reveal these defects, indicating their microscopic and localized nature. Larger scale defects or defect concentrations could lead to the mechanical failure of the membrane during temperature cycling, which is not observed. For fuel cells with thick electrolytes, the mismatch of thermal expansion between electrodes and electrolyte can lead to catastrophic failure. Structural defects for oxide-based electrode materials can also be induced by volumetric changes caused by variations in point defect concentration or stoichiometry as noted in literature [21-24]. For the specific case of our vanadium and vanadium oxide anodes in thin film solid oxide fuel cells, the open circuit potential dependence on as-deposited stoichiometry could be due to the relative importance of these volumetric changes during operation. The mechanical behavior of freestanding oxide electrolytes can contribute to lower the open circuit potential difference of thin film solid oxide fuel cells [25].

We first consider thermal expansion mismatch between vanadium oxide electrodes with different stoichiometries and the YSZ electrolyte. The mismatch strain ($\Delta\varepsilon$) between the vanadium oxide electrode and the YSZ electrolyte at temperature T, is equal to:

$$\Delta\varepsilon = \int_{T_0}^{T} [\alpha_{an}(T) - \alpha_{YSZ}(T)]dT$$

with T_0 = 295 K, α_{an} the coefficient of thermal expansion of the anode and α_{YSZ} the coefficient of thermal expansion of the electrolyte. Our estimation does not take into account thermal expansion of the porous metal cathode nor the presence of a surface layer formed during exposure of the anode to air as revealed by XPS measurements. The metal is relatively compliant while the surface layer thickness is small compared to total anode thickness. The coefficients of thermal expansion of the electrodes used for the calculations are from dilatometry and x-ray diffraction measurements on bulk vanadium and vanadium oxides [26-33], and the coefficient of thermal expansion of the electrolyte is estimated from internal stress measurements during temperature cycling of yttria-stabilized zirconia thin films on silicon substrates [34]. The average thermal expansion coefficients extracted from the literature are summarized in Table 1. Due to anisotropy of most vanadium oxide crystals,

we consider the average strain $e = (e_{11}+e_{22}+e_{33})/3$ that would result from expansion of polycrystalline vanadium oxide films such as in our fuel cells. For VO_2, we also include the expansion resulting from the monoclinic to tetragonal transformation at 341 K. The calculated thermal expansion mismatch strains for V, VO, V_2O_3, VO_2 and V_2O_5 on YSZ are shown in Figure 6. The thermal expansion mismatch strain is positive for VO, V_2O_3 and V_2O_5 and negative for V and VO_2. At temperatures relevant for fuel cell operation, the absolute values of mismatch strain increase in the order V, VO, V_2O_3, V_2O_5 and VO_2. Interestingly, we observe that V_2O_3 and V_2O_5 have positive mismatch strain with YSZ and have near-ideal open circuit potential at temperatures higher than 640 K.

Second, we evaluate the equilibrium vanadium oxide composition to account for high-temperature phase transformations at the anode. Equilibrium calculations of different vanadium oxide compositions with H_2-H_2O mixtures were performed with the HSC Software Package [13]. Stability domains are derived from thermodynamic data for water, oxygen, hydrogen, vanadium and vanadium oxides, available for the whole temperature range considered here. The most stable vanadium oxide phase for given temperature, hydrogen and water partial pressure is determined by minimization of the Gibbs free energy. The thermodynamic properties used for the equilibrium calculations are summarized in Table 2 and the calculation results are shown in Figure 7. We conclude from these that V_2O_3 is the most stable oxide in our fuel cell operating temperature range, when exposed to the 3% H_2O-5% H_2-Ar anode ambient in our experiments. To check the validity of our thermodynamic analyses, we compared them to literature data collected from different sources. The equivalent p_{O2}, calculated from the equilibrium constant of $2\ H_{2(g)} + O_{2(g)} = 2\ H_2O_{(g)}$ varies from 5×10^{-51} at 423 K to 7×10^{-24} Pa at 773 K. At these p_{O2} values, Richardson-Ellingham diagrams calculated by others also confirm V_2O_3 is the most stable phase for this range of temperature and p_{O2} values [35]. The similarities in oxidation state of the vanadium in the anodes, determined by XPS after operation (Fig. 5), for initially more oxidized or reduced vanadium indicate that the anodes eventually equilibrated with the fuel at high temperature. Differences in performance persist inspite

of the compositional changes that occur during operation. The oxidation or reduction of the various anode composition systems to V_2O_3 would be accompanied by volume changes, inducing additional mismatch strain between the anode and electrolyte films. The magnitude of the mismatch strain is expected to be much larger than that due to thermal expansion mismatch. This could account for the fact that the as-deposited V_2O_3 anode has near ideal open-circuit potential. A future study to expand this work could evaluate the overall stress evolution *in situ*. This would consider possible stress relaxation mechanisms occurring here during high temperature operation: for instance, only 10 % of crystallization-induced volumetric changes result in stresses for amorphous-crystalline transitions taking place at 423 K in some phase change materials [36].

5. Conclusions

We have fabricated thin film solid oxide fuel cells with different vanadium oxide anode compositions, with as-deposited stoichiometry varied from V to V_2O_5. The best performing cells having near-ideal open circuit potential had either V_2O_3 or V_2O_5 anodes before operation in hydrogen. After operation with hydrogen fuel, XPS revealed similar anode stoichiometries, due to equilibration of the anode with the fuel composition. Phase stability under operating conditions was investigated by thermodynamic calculations. The observed experimental trends were discussed considering the role of thin film stresses and structural changes that occur during the high temperature operation. This strategy could be extended to obtain near-ideal open circuit potential with other electrode materials particularly as they are incorporated into suspended membranes for intermediate temperature operation.

ACKNOWLEDGMENT QVO acknowledges financial support from the F.R.S.-FNRS through a postdoctoral scholarship. This work was performed in part at the Harvard University Center for Nanoscale Systems (CNS) a member of the National Nanotechnology Infrastructure Network (NSF award no. ECS-0335765) and at the MRSEC Shared Experimental Facilities at MIT (NSF award no. DMR-08-19762).

REFERENCES

[1] H. Huang, M. Nakamura, P. Su, R. Fasching, Y. Saito, F.B. Prinz, J. Electrochem. Soc. 154 (2007) B20-B24.

[2] A. Bieberle-Hütter, D. Beckel, A. Infortuna, U. P. Muecke, J.L.M. Rupp, L.J. Gauckler, S. Rey-Mermet, P. Muralt, N.R. Bieri, N. Hotz, M.J. Stutz, D. Poulikakos, P. Heeb, P. Müller, A. Bernard, R. Gmür, T. Hocker, J. Power Sources 177 (2008) 123-130.

[3] U.P Muecke, D. Beckel, A. Bernard, A. Bieberle-Hütter, S. Graf, A. Infortuna, P. Müller, J.L.M. Rupp, J. Schneider, L.J. Gauckler, Adv. Func. Mater. 18 (2008) 3158.

[4] S.H. Choi, C.S. Hwang, M.H. Lee, ECS Electrochem. Lett. 3 (2014) F57-F59.

[5] B.-K. Lai, K. Kerman, S. Ramanathan, J. Power Sources 196 (2011) 1826-1832.

[6] A. C. Johnson, B.-K. Lai, H. Xiong, S. Ramanathan, J. Power Sources 186 (2009) 252-260.

[7] I.E. Wachs, Dalton Trans. 42 (2013) 11762-11769.

[8] S. Tepavcevic, H. Xong, C.R. Stamenkovic, X. Zuo, M. Balasubramanian, V.B. Prakapenka, C.S. Johnson, T. Rajh, ACS Nano 6 (2012) 530-538.

[9] Y. Yufit, B. Hale, M. Matian, P. Mazur, N.P. Brandon, J. Electrochem. Soc. 160 (2013) A856-A861.

[10] S. Nordlinder, K. Edström, T. Gustafsson, Electrochem. Solid-State Lett. 4 (2001) A129-A131.

[11] Q. Van Overmeere, K. Kerman, S. Ramanathan, Nano Lett. 12 (2012) 3756-3760.

[12] K. Kerman, B.-K. Lai, S. Ramanathan, J. Power Sources 196 (2011) 2608-2614.

[13] A. Roine, HSC Chemistry 6.12, Outokumpu Research Oy: Pori, Finland, 2007.

[14] I. Safi, Surf. Coatings Technol. 127 (2000) 203-219.

[15] G. Silversmit, D. Depla, H. Poelman, G.B. Marin, R. De Gryse, Surf. Sci. 600 (2006), 3512-3517.

[16] G. Silversmit, D. Depla, H. Poelman, G.B. Marin, R. De Gryse, J. Electron Spectrosc. Relat. Phenom. 135 (2004) 167-175.

[17] M.C. Biesinger, L.W.M. Lau, A.R. Gerson, R.St.C. Smart, Appl. Surf. Sci. 257 (2010) 887-898.

[18] E. Hryha, E. Rutqvist, L. Nyborg, Surf. Interface Anal. 44 (2012) 1022-1025.

[19] R. Lindström, V. Maurice, S. Zanna, L. Klein, H. Groult, L. Perrigaud, C. Cohen, P. Marcus, Surf. Interface Anal. 38 (2006) 6-18.

[20] V. Balakrishnan, C. Ko, S. Ramanathan, J. Mater. Res. 27 (2012) 1476-1481.

[21] S.B. Adler, J. Am. Ceram. Soc. 84 (2001) 2117-2119.

[22] S.R. Bishop, K.L. Duncan, E.D Wachsman, Electrochim. Acta 54 (2009) 1436-1443.

[23] Q. Yang, T.E. Burye, R.R. Lunt, J.D. Nicholas, Solid State Ionics 249-250 (2013) 123-128.

[24] A.Kossoy, Y. Feldman, E. Wachtel, I. Lubomirsky, J. Maier, Adv. Func. Mater. 17 (2007) 2393.

[25] K. Kerman, Q. Van Overmeere, M. Karpelson, R.J. Wood, S. Ramanathan, ACS Nano 7 (2013) 10895-10903.

[26] N. Schmitz-Pranghe, P. Dünner Z. metallkunde 59 (1968) 377.

[27] I.I. Mechnikov, Izvestiya Vysshikh Uchebnykh Zavedenii Fizika 12 (1969) 65-68.

[28] A. Taylor, N.J. Doyle, J. Appl. Cryst. 4 (1971) 103-109.

[29] L.J. Eckert, R.C. Bradt, J. Appl. Phys. 44 (1973) 3470-3472.

[30] B. Belbéoch, R. Kleinberger, M. Roulliay, Solid State Commun. 25 (1978) 1043-1044.

[31] D. Kucharczyk, T. Niklewski, J. Appl. Cryst. 12 (1979) 370-373.

[32] K.V.K. Rao, S.V.N. Naidu, L. Iyengar, J. Phys. Soc. Jpn. 23 (1967) 1380.

[33] T.N. Kennedy, R. Hakim, J.D. McKenzie, Mater. Res. Bull. 2 (1967) 193-200.

[34] D.J. Quinn, "Microstructure, residual stress, and mechanical properties of thin film materials for a microfabricated solid oxide fuel cell", Ph.D. Thesis (p. 156), Massachusetts Institute of Technology (2006).

[35] I. Yamaguchi, T. Manabe, T. Tsuchiya, T. Nakajima, M. Sohma, T. Kumagai, Jpn. J. Appl. Phys. 47 (2008) 1022-1027.

[36] T.P. Leervad Pedersen, J. Kalb, W.K. Njoroge, D. Wamwangi, M. Wuttig, F. Spaepen, Appl. Phys. Letters 79 (2001) 3597.

[37] I. Barin, O. Knacke, O. Kubaschewski, Thermochemical properties of inorganic substances, Supplement, Springer-Verlag, Berlin (1977) 861.

[38] Thermodynamic Data for Fifty Reference Elements, NASA-TP-3287, N93-19977, 1993.

[39] Landolt-Börnstein: Thermodynamic Properties of Inorganic Material, Scientific Group Thermodata Europe (SGTE), Springer-Verlag, Berlin-Heidelberg, 1999.

[40] I. Barin, Thermochemical Data of Pure Substances, VCH Verlags Gesellschaft, Weinheim (1989).

[41] M. Chase, NIST-JANAF, Thermochemical Tables - Fourth Edition, J. of Phys. and Chem. Ref. Data, Mononograph No. 9, 1998.

[42] M. Binnewies, E. Milke, Thermochemical Data of Elements and Compounds, 2nd edition, Wiley-VCH, Weinheim, 2002.

[43] O. Knacke, O. Kubaschewski, K. Hesselman, Thermochemical properties of inorganic substances, 2nd ed., Springer-Verlag, Berlin, pp.1-1113, 1991.

[44] Scientific Group Thermodata Europe, Grenoble Campus, 1001 Avenue Centrale, BP 66, F-38402 Saint Martin d'Héres, France, 1994.

[45] Glushko Thermocenter of the Russian Academy of Sciences, IVTAN Association, Izhorskaya 13/19, 127412 Moscow, Russia, 1994.

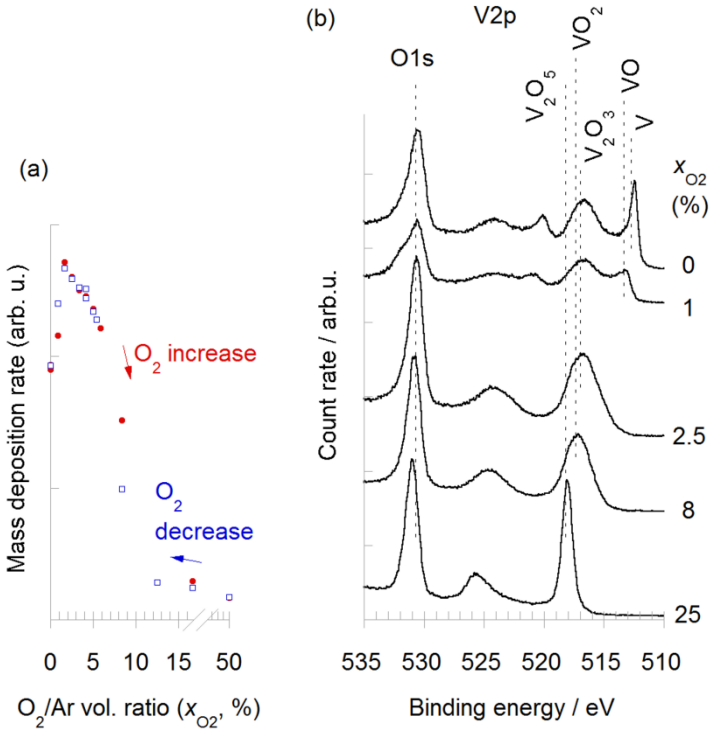

Figure 1. (color online) (a) Variation of the deposition rate when increasing (filled circles) and decreasing (empty squares) the oxygen-to-argon ratio during reactive sputtering of vanadium oxide (b) X-ray induced photoelectron spectra of vanadium oxide films deposited by reactive sputtering at different oxygen partial pressures. The spectra are shifted for clarity.

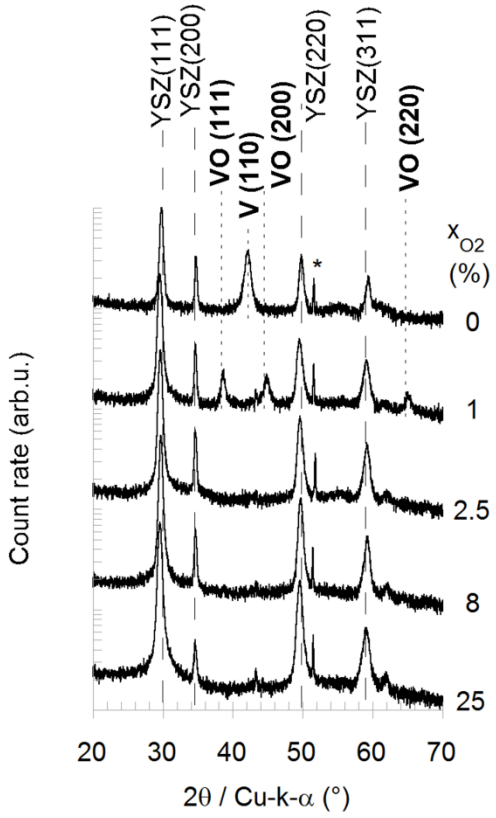

Figure 2. Grazing incidence X-ray diffractograms of vanadium oxide films deposited by reactive sputtering at different oxygen partial pressures. The diffraction peaks are indexed to V (ICDD 00-022-1058) and VO (ICDD 01-077-2173). Remaining peaks correspond to a polycrystalline cubic yttria-stabilized zirconia film deposited prior the vanadium oxide film (ICDD 00-030-1468). The sharp peak, labeled with an asterisk, likely results from dynamic diffraction from the silicon substrate in the grazing incidence geometry. Diffractograms are shifted for clarity.

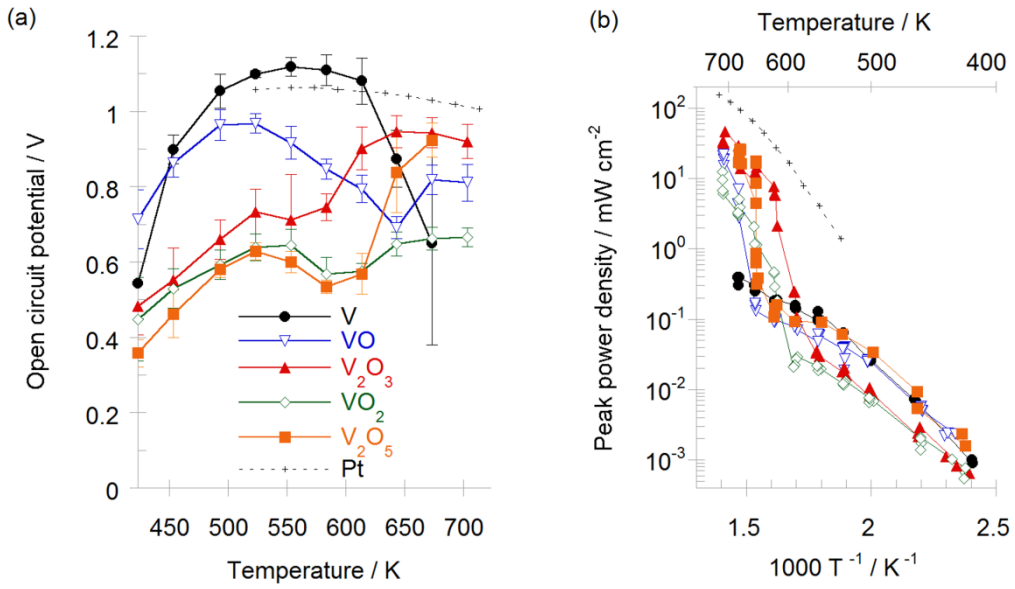

Figure 3. (color online) (a) Open circuit potential and (b) peak power density for different as-deposited vanadium oxide stoichiometries, as a function of temperature. The performance of a porous Pt anode fuel cell is included for comparison. Open circuit potentials are averaged over nine fuel cells per data point, excluding shorted cells for which the open circuit potentials are lower than 0.05 V. These cells are also excluded for Figure 3 (b).

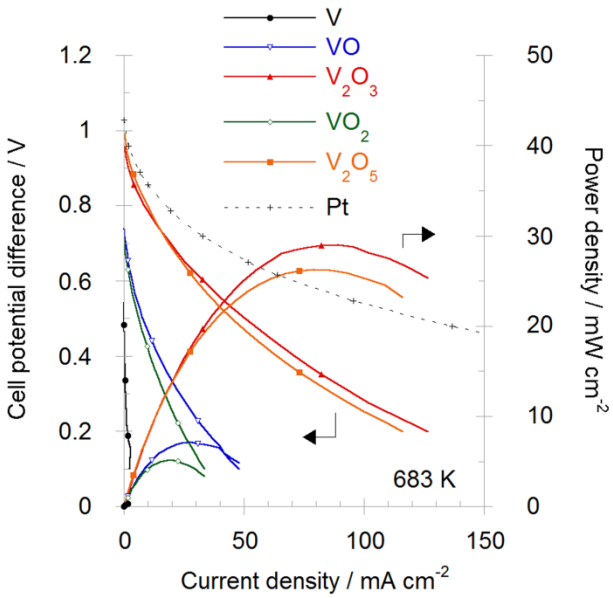

Figure 4. (color online) Operational curves for the thin film solid oxide fuel cell with vanadium oxide anodes with different as-deposited stoichiometries at 683 K. The performance of a comparable cell with porous Pt anode fuel cell is included for comparison.

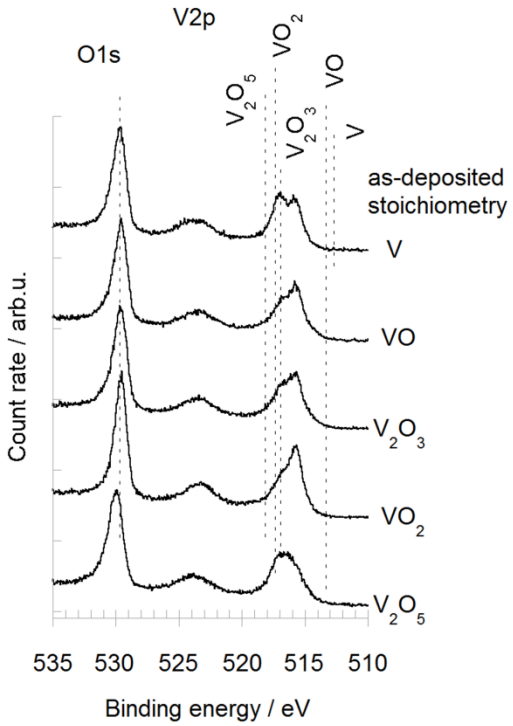

Figure 5. V2p and O1s XPS spectra of the vanadium oxide anodes after fuel cell operation in room temperature humidified 5% H_2/Ar up to 713 K and cool down with flowing fuel. The stoichiometries correspond to the anodes in the as-deposited state.

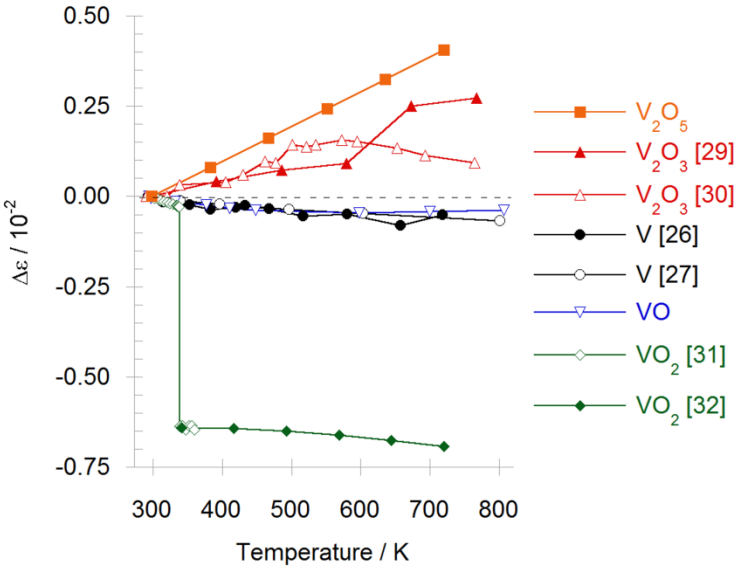

Figure 6. (color online) Predicted thermal-induced strain difference between different vanadium oxide stoichiometries and yttria-stabilized zirconia. References from which data are extracted are indicated.

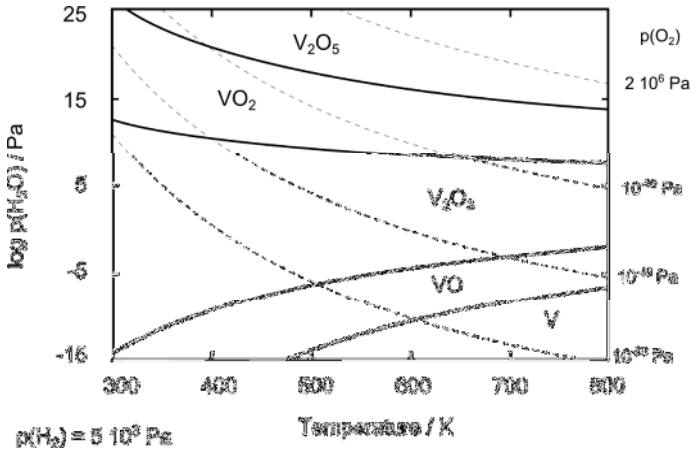

Figure 7. Equilibrium vanadium oxide compositions as a function of temperature and partial water pressure at a fixed hydrogen partial pressure of 5% and atmospheric pressure. The thermodynamic data used for the calculations is summarized in Table 2. V_2O_3 is predicted to be the most stable phase in the environment of the anode consisting of 3% H_2O-5% H_2- Ar for the temperature range used throughout the study. Dashed lines are iso-partial oxygen pressure lines, calculated from the equilibrium constant values of the $2\ H_2 + O_2 = 2\ H_2O$ reaction.

Table 1. Average coefficients of thermal expansion (CTE) of bulk vanadium, bulk vanadium oxides and yttria-stabilized zirconia thin films (YSZ) from the reference data used to calculate the thermally-induced mismatch strain between the vanadium oxide anode and the YSZ electrolyte.

	Average CTE / 10^{-6} K^{-1}	References and notes
YSZ	12.2 (298...773 K)	[34]. Calculated with Young modulus of 120 GPa and Poisson ratio of 0.3 from Quinn et al.'s data. YSZ film deposited at 600°C.
V	10.9 (293...718 K)	[26]. Calculated from lattice spacing vs. T.
	11.6 (295...800 K)	[27]. Calculated from dilatometry data.
VO	11.4 (293...800 K)	[28]. Calculated from lattice spacing vs. T.
V_2O_3	21.4 (298...770 K)	[29]. Calculated from fit of lattice spacings vs. T.
	15.0 (290...770 K)	[30]. Calculated from unit cell volume vs. T.
VO_2	5.2 (298...338 K) 8.8 (339...360 K)	[31] Calculated from lattice parameters vs. T.
	13.4 (341...720 K)	[32] Calculated from fit of unit cell CTE vs. T.
V_2O_5	21.8 (323...873 K)	[33]. Calculated from average unit cell CTE. (α_a = 2.0, α_b = 55.4, α_c = 8.0) 10^{-6} K^{-1}.

Table 2. Summary of the vanadium oxide stoichiometries considered for the equilibrium calculation and their relevant thermodynamic properties, with original references for the thermodynamic data. The heat capacity c_p is calculated with $c_p = A + BT + CT^{-2} + DT^2$ in the specified temperature ranges.

	H^0 / kJ mol^{-1}	S^0 / J $mol^{-1}K^{-1}$	A / J mol^{-1} K^{-1}	B / 10^{-3} J mol^{-1} K^{-1}	C / 10^5 J mol^{-1} K^{-1}	D / 10^{-6} J mol^{-1} K^{-1}	T range for c_p (K)	Ref.
V	0	0	1.078	1.762	-0.03	-1.660	300 to 450	[37-39]
	0	0	1.754	-0.516	-0.215	0.514	450 to 800	[38]
VO	-24.67	2.228	3.023	0.749	-0.935	0	300 to 800	[40-42]
V_2O_3	-69.622	5.604	8.243	-1.066	-1.968	0.622	300 to 800	[40-42]
VO_2	-40.762	2.956	1.289	8.933	0.001	-6.129	300 to 340	[43,44]
	0.257	0.756	3.937	1.088	-0.704	-0.425	340 to 700	[43,44]
	0	0	4.175	0.491	-0.868	0.010	700 to 800	[44]
V_2O_5	-88.599	7.455	10.907	-5.308	-2.231	5.445	300 to 800	[40,45]